Experimental Reduction of Laser Imprinting and Rayleigh–Taylor Growth in Spherically Compressed, Medium-*Z*–Doped Plastic Targets

Introduction

The performance of inertial confinement fusion (ICF) ignition targets[1,2] can be compromised by implosion asymmetries caused by hydrodynamic instabilities. If the target deformation is large enough, it causes mixing of the inner hot area of the target ("hot spot") with the outer colder shell, quenching the fusion reactions. The Rayleigh–Taylor (RT) instability[3] is the primary hydrodynamic instability that develops during the compression of an ICF capsule. Small nonuniformities, seeded at the outer ablation interface by imperfections in the laser irradiation and/or by target surface roughness, are amplified during the acceleration phase, feed through the shell, and seed the RT growth at the inner surface of the shell, which becomes unstable during the stagnation phase.

Because of the paramount importance of this instability to the success of ICF, a great amount of theoretical and experimental research has been devoted to reducing the seed nonuniformities and mitigating the instability growth. To reduce the initial beam imprint and improve the laser radiation uniformity, LLE's OMEGA Laser System[4] employs 60 beams on the surface of a spherical capsule augmented by advanced nonuniformity reduction techniques such as laser-beam two-dimensional (2-D) smoothing by spectral dispersion (SSD),[5] distributed phase plates (DPP's),[6] polarization smoothing (DPR),[7] and temporal shaping of the laser pulse.[8,9]

Techniques for RT mitigation such as coating the target with a high-*Z* material and the shell's volumetric doping with impurities have been studied elsewhere.[10–13] Radiation preheat, enhanced by impurities, reduces the peak density, increases the ablation velocity, and increases the density-gradient scale length; all of which decrease the RT growth rate.[14] Expansion of the ablated doped plasma reduces the laser imprint by increasing the separation between the absorption region and the ablator surface. Experiments with planar targets in the Nike facility demonstrated reduction of the instability for targets coated with thin Pd or Au layers.[11] On OMEGA, coating deuterium-filled plastic spherical capsules with a thin layer of palladium resulted in a twofold increase in the neutron yield.[12] Capsules volumetrically doped with Si and Ge were imploded and their neutron yield doubled as well.[13]

This article presents time-resolved measurements of the RT growth of target areal-density modulations during the spherical implosion of thin plastic shells volume doped with Si and Ge. The targets were imploded with 48 laser beams with a low-adiabat, triple-picket laser pulse shape[8] with an intensity of 4×10^{14} W/cm^2 and a duration of 2.5 ns. To seed the initial nonuniformities, SSD[5] was turned off. The targets were backlit with x rays generated by irradiating a Ta backlighter target with six overlapping beams with the same pulse shape. The x rays passing through the shell were recorded by a fast framing camera,[15] and the density (areal density) perturbation of the shell was inferred from the x-ray absorption.[16] The results indicate that the initial perturbation amplitude at the beginning of the compression phase was reduced by a factor of 2.5±0.5 for CH [4.3% Si] targets and by a factor of 3±0.5 for CH [7.4% Si] and CH [3.9% Ge] targets. At the end of compression the reduction factor in the density modulation became 3±0.5 and 5±0.5, respectively. The instability growth rate was reduced by a factor of 1.5 in doped targets in comparison to undoped ones. These results agree with simulations using the 2-D, radiation–hydrodynamics code *DRACO*.[17]

This article is organized as follows: The experimental configuration is described; the main results are presented; and the discussion is summarized.

Experimental Configuration

The experimental configuration, diagnostics, and data analysis are similar to those described in Refs. 16, 18, and 19. The experimental setup is illustrated in Fig. 130.56. The targets were smooth spherical plastic (CH) shells with an outer diameter of 860 μm and a shell thickness of 22 μm. Pure plastic shells and plastic shells volumetrically doped with Si (4.3% and 7.4%) and Ge (3.9%) were used. The targets were irradiated with 48 OMEGA beams (out of the remaining 12 beams, six beams were used for backlighter irradiation and six beams incident on the diagnostic hole in the target were not used) with

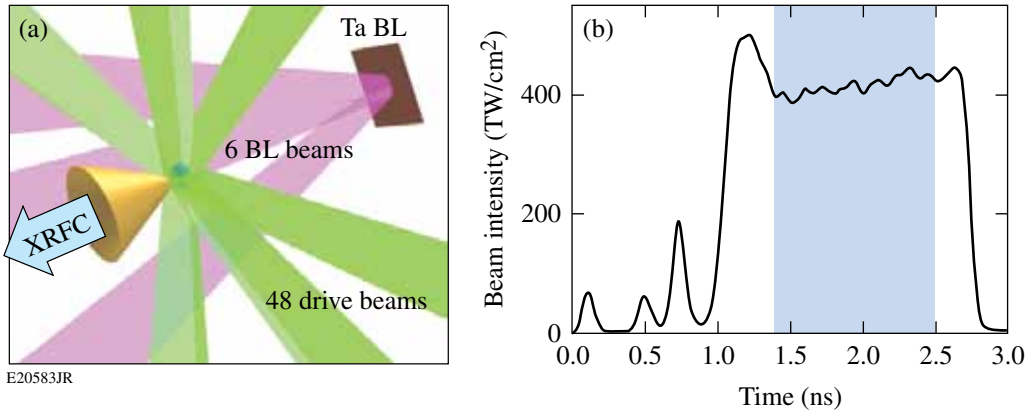

Figure 130.56
(a) Experimental setup. A spherical plastic shell was imploded by 48 beams (green) and the Ta backlighter (BL) was irradiated by 6 beams (violet). The shells had an outer diameter of 860 μm and a thickness of 22 μm. Each shell had a round opening with a diameter of 400 μm into which was inserted a gold cone shield with a tip opening of 400 μm, a height of 3 mm, and an opening angle of 53°. A Ta foil backlighter ($500 \times 500 \times 20$ μm^3) was placed 9 mm from the target. The target was x-ray radiographed by an x-ray framing camera (XRFC) during a time interval of 1.4 ns to 2.5 ns. (b) Laser power shape. The measurement interval from 1.4 ns to 2.5 ns is highlighted.

the triple-picket pulse laser shape at a total energy of 14.4 kJ (300 J per beam) and a main drive time duration of 2.5 ns. To seed the initial nonuniformities, SSD was turned off. The shells were backlit by x rays from a Ta foil backlighter ($500 \times 500 \times 20$ μm^3) placed 9 mm from the target and irradiated with six beams with the same pulse shape.

Similar to Ref. 19, the shells had a round opening with a diameter of 400 μm through which one could monitor the transmission of the x rays through the shell. To shield the opening and the line of sight against direct x-ray exposure from the coronal plasma, a gold cone with a tip opening of 400 μm, a height of 3 mm, and an opening angle of 53° was inserted into the shell's opening.

The x rays, with a peak energy of about 2.8 keV, were recorded with a fast x-ray framing camera (XRFC),[15] and the shell's areal-density variation was inferred from spatial modulation of the x-ray transmission. The camera's 16-pinhole array was situated at 3 cm from the target and the images were recorded with a charge-coupled device (CCD) situated at a distance of 36 cm from the pinhole array. The pinholes had a diameter of 10 μm, and the CCD had 2048×2048 pixels with a size of 18 μm $\times$ 18 μm each. This viewing geometry resulted in a magnification of 12 and provided a field of view at the shell's surface of approximately 400 μm in diameter. The modulation transfer function (MTF) of the imaging system was 50% at a wavelength of approximately 20 μm and 10% at a wavelength of approximately 10 μm, the latter representing the limit of spatial resolution. The framing camera was triggered at 1.4 ns, and 16 images were recorded during a time interval of 1.4 ns to 2.5 ns [highlighted in Fig. 130.56(b)] with a frame-to-frame time interval of ~60 ps.

Experimental Results

1. X-Ray Absorption

Attenuation of x rays with a reasonably narrow spectrum (the measured spectrum had a relative width $\Delta E/E \approx 20\%$) can be described as $I = I_{\mathrm{BL}} \exp\left(-\bar{\mu}\rho\delta\right)$, where ρ and δ are correspondingly the shell's mass density and thickness, $\bar{\mu}$ is the spectrum-averaged mass attenuation coefficient, and I_{BL} is the backlighter intensity. To measure the x-ray absorption in the shell, a series of shots were conducted using undriven shells that had laser-drilled, round, 200-μm-diam openings facing the backlighter. In a single shot, within the 400-μm field of view set by the framing camera, the intensities of x rays passing unattenuated through the 200-μm opening and attenuated through the shell were compared. The mass attenuation coefficient was calculated as $\bar{\mu} = (\rho\delta)^{-1} \ln\left(I_{\mathrm{open}}/I_{\mathrm{shell}}\right)$, where I_{open} and I_{shell} are, respectively, the x-ray intensities passing through the opening and the shell and δ is the shell thickness. The values for the mass attenuation coefficients obtained are given in Table 130.III. To simplify further notations, the bar sign over $\bar{\mu}$ will be omitted.

2. Areal-Density Modulation

For the shell-density modulation measurement, SSD beam smoothing was turned off so the laser beams' speckle created a broadband spectrum of seed-density perturbation at the time of the first picket. The areal-density modulation was determined

Table 130.III: Measured mass attenuation coefficient for undoped (CH) and doped shells. The amount and type of doping were 4.3% Si, 7.4% Si, and 3.9% Ge.

	CH	CH [4.3% Si]	CH [7.4% Si]	CH [3.9% Ge]
(g/cm^3)	1.02	1.07	1.29	1.34
$\bar{\mu}\left(\mathrm{cm}^2/\mathrm{g}\right)$	110±26	317±50	420±67	517±62

by taking a natural logarithm of the modulation of the image intensity I:

$$\ln I = \ln I_{\mathrm{BL}} - \mu\rho r, \tag{1}$$

where I_{BL} is the backlighter intensity. The product $\mu\rho r$ is commonly called optical density (OD). A typical image of the natural ln of XRFC intensity taken at $t = 2.12$ ns is shown in Fig. 130.57. A CH target doped with 3.4% of Si was used.

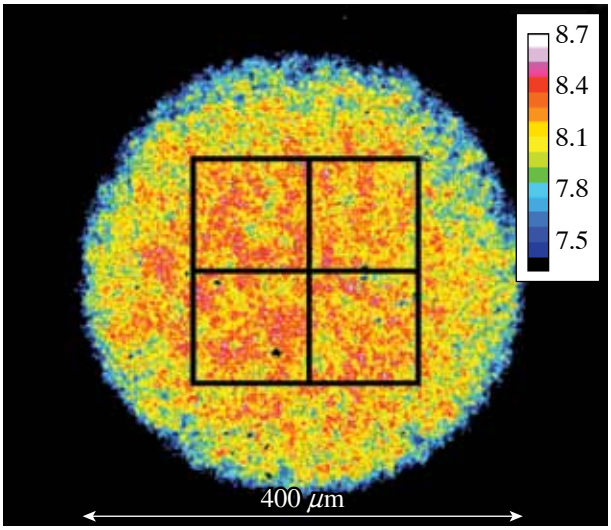

E20584JR

Figure 130.57
An XRFC image of ln(I) for a CH target doped with 4.3% Si taken in t = 2.12 ns. The size of the image is approximately 400 μm. The large 192 × 192-μm^2 square (128 × 128 pixels) was used to calculate modulation rms. The four 96 × 96-μm^2 subregions were used to calculate error.

As the first step of data analysis, high-frequency digital noise in the XRFC signal was reduced by smoothing over two CCD pixels, equivalent to filtering out spatial frequencies higher than 300 mm^{-1}. Large-scale variations of the backlighter intensity were removed using 2-D, fourth-order polynomial fitting to ln$I$ (Ref. 18). Equation (1) describes the remaining fine-scale spatial modulation of the areal density ρr and the optical density (OD) $\mu\rho r$.

One way to characterize the density modulation is to calculate its rms (root-mean-square) value averaged over a certain area. A region of interest (ROI) of 128 × 128 pixels selected in each image corresponds to a 192 × 192-μm^2 area at the shell's surface (Fig. 130.57). Each ROI was subdivided into four smaller ROI's, 64 × 64 pixels each, and the rms calculation (described below) was repeated for each subregion. The standard deviation of results obtained for each subregion is considered as the measurement error represented by the "error bars" in the figures that follow.

The modulation of the backlighter intensity and the shell density are assumed to be uncorrelated. Therefore, the rms of the signal intensity fluctuations is comprised of the rms of the shell's optical-density modulation added in quadrature to the rms of the backlighter modulation:

$$\sigma^2_{\ln I} = \sigma^2_{\mathrm{OD}} + \sigma^2_{\ln I_{\mathrm{BL}}}. \tag{2}$$

The second term in the right-hand side of Eq. (2) can be treated as the background or the noise floor of the measurement and is subtracted from the signal rms to obtain the true rms of the areal-density modulation. Because the backlighter intensity varies with time for each shot and changes from shot to shot, the background subtraction must be done carefully. To scale the background noise with the mean intensity of the transmitted x rays, a series of shots with undriven shells was performed, so the density fluctuation was absent and any fluctuation of the signal resulted from modulation of the backlighter intensity (and statistical noise). This dependence (shown in Fig. 130.58) is fitted by a power fit $\sigma^2_{\ln I_{\mathrm{BL}}} = 0.46\,\bar{I}^{-0.59}$, where $\bar{I}$ is the mean value of the transmitted intensity. Using Eq. (2) the rms of the areal-density modulation is

$$\sigma_{\rho r} = \mu^{-1}\sigma_{\mathrm{OD}} = \mu^{-1}\sqrt{\sigma^2_{\ln I} - 0.46\,\bar{I}^{-0.59}}. \tag{3}$$

The time evolution of the areal-density perturbation for undoped and doped targets is shown in Fig. 130.59 and compared with simulations using the 2-D, radiation–hydrodynamics code *DRACO*[17] (shown as solid lines). Cross-beam energy

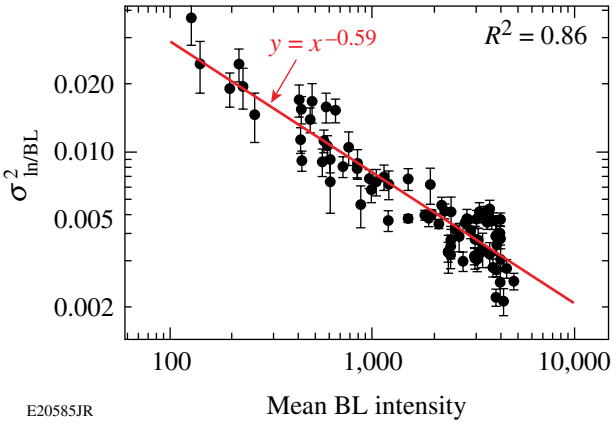

Figure 130.58
Measured rms of backlighter intensity as a function of mean backlighter intensity. A power fit is shown as the red line.

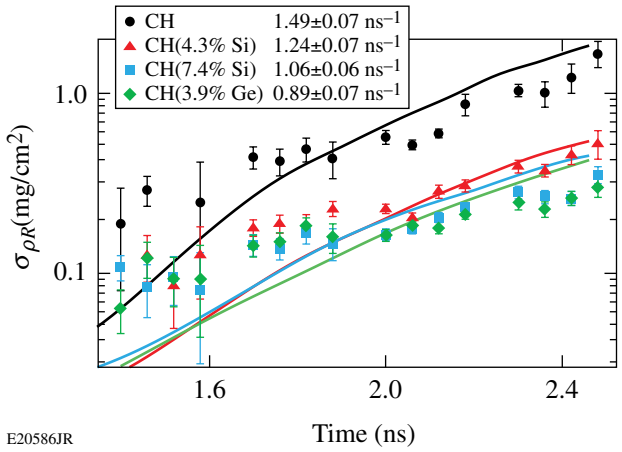

Figure 130.59
The time evolution of the areal-density perturbation amplitude for undoped and doped targets. The symbols are the measured data and the solid lines of the same color are the *DRACO* calculations. The corresponding measured growth rates, calculated as the slopes of the respective exponential fits, are shown in the legend box.

transfer (CBET)[20] was taken into account, providing a slightly reduced drive.

The initial perturbation amplitude at the beginning of the acceleration phase was reduced by a factor of 2.5±0.5 for CH [4.3% Si] targets and by a factor of 3±0.5 for CH [7.4% Si] and CH [3.9% Ge] targets. At the end of compression the reduction factor in the density modulation becomes 3±0.5 and 5±0.5, correspondingly. All targets exhibit exponential perturbation growth, and their growth rates are calculated as the slopes of the respective exponential fits. The doped targets demonstrate a reduction in the growth rate from ≈1.5 ns^{-1} for pure-CH targets to ≈0.9 ns^{-1} for targets doped with 3.9% Ge. The reduction in the growth rate also agrees well with the growth rates for the dominant wavelengths calculated by *DRACO*: 1.46 ns^{-1} for pure-CH targets and 0.92 ns^{-1} for targets doped with 3.9% Ge. A more-detailed comparison can be found in Ref. 21.

The 2-D simulations reproduce the experimental trend of reduction in modulation and the growth rate reasonably well except at the beginning of acceleration when the measured perturbations are somewhat larger than predicted by *DRACO*. The discrepancy could be caused by a small signal amplitude and a large noise contribution at the beginning of acceleration. A similar deviation was observed in earlier spherical compression experiments.[19] At the end of the acceleration phase, the signal is much larger and agreement with numerical simulations is much better.

3. Spectral Composition

To gain insight into the structure of the shell's density modulation, its spatial power spectrum is calculated by performing 2-D, MTF-corrected Fourier decomposition. Typical power spectra for driven and undriven CH spherical targets are shown in Fig. 130.60 as functions of the spatial frequency. As expected, the driven and undriven spectra merge at a frequency corresponding to the MTF-limited resolution. The difference between the two power spectra is the spectrum of the areal-density fluctuation. The power spectra of the optical-density modulation for CH [3.9% Ge] targets at different times are shown in Fig. 130.61. The power spectra calculated by *DRACO* are shown in the same plots and are in reasonable agreement

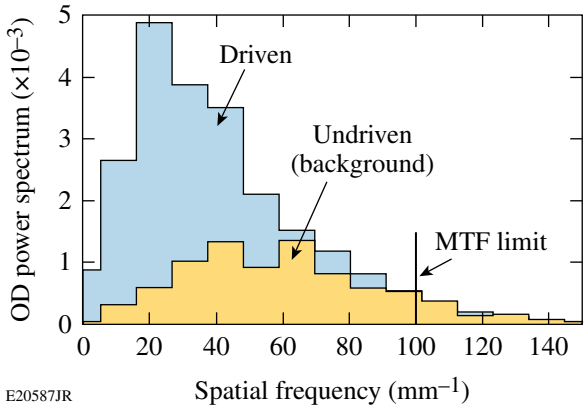

Figure 130.60
Spatial power spectra of optical-density modulation for undriven and driven spherical CH targets at t = 2.4 ns. The undriven target's modulation is caused by the nonuniformities in the backlighter radiation and is subtracted from the driven target's modulation to obtain the modulation in the shell's areal density.

with the measured spectra. The results indicate that during the acceleration phase, the spectral power is shifting from high spatial frequencies (short wavelengths) at the beginning to shorter spatial frequencies (long wavelengths) later in time, similar to what was observed for planar targets.[22,23]

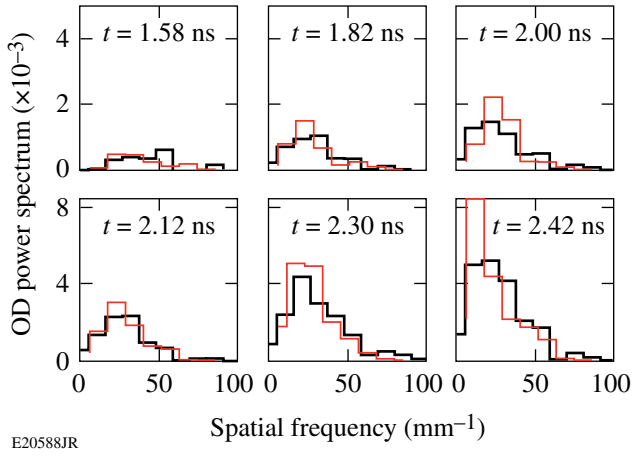

Figure 130.61
Plots of OD power spectra for CH [3.9% Ge] spherical targets at different times. The measured spectra are shown as thick (black) lines and the calculated spectra are shown as thin (red) lines.

Discussion and Conclusions

The experiments have demonstrated that doping plastic shells with a several-percent concentration of medium-Z impurity such as Si or Ge substantially decreases the initial imprint and the growth rate, leading to a significant reduction of the shell's areal-density perturbation. The initial perturbation amplitude at the beginning of the compression phase was reduced by a factor of 2.5±0.5 for CH [4.3% Si] targets and by a factor of 3±0.5 for CH [7.4% Si] and CH [3.9% Ge] targets. At the end of compression the reduction factor in the density modulation becomes 3±0.5 and 5±0.5, correspondingly. The doped targets demonstrate a reduction in the growth rate from ≈1.5 ns^{-1} for pure-CH targets to ≈0.89 ns^{-1} for targets doped with 3.9% Ge. The results agree well with numerical simulations using *DRACO*. From the analysis of the simulation results described in Ref. 21, the main mechanisms of the growth suppression are (a) an increase in the stand-off distance between the laser-absorption region to the ablation front and (b) enhanced coronal radiation preheating in doped shells. The simulations show that the ablation velocity increases from V_a = 5.95 μm/s for CH targets to V_a = 13.5 μm/s for CH [3.9% Ge] targets, which reduces the RT linear growth rate according to the fitting formula[14] $\gamma_k = 0.94\sqrt{kg/(1+kL_n)} - 1.5\,kV_a$, where k is the modulation wave vector, g is the acceleration, and L_n is the gradient length. Ignition-scale direct-drive target designs would require doping only the outer half of the ablator material to prevent excessive radiation preheating of the main fuel. Future experiments will address the imprint reduction effects in shells with the dopant introduced only into the outer layer of the ablator.

ACKNOWLEDGMENT

This work was supported by the U.S. Department of Energy Office of Inertial Confinement Fusion under Cooperative Agreement No. DE-FC52-08NA28302, the University of Rochester, and the New York State Energy Research and Development Authority. The support of DOE does not constitute an endorsement by DOE of the views expressed in this article.

REFERENCES

1. J. D. Lindl, *Inertial Confinement Fusion: The Quest for Ignition and Energy Gain Using Indirect Drive* (Springer-Verlag, New York, 1998).
2. J. D. Lindl, R. L. McCrory, and E. M. Campbell, Phys. Today **45**, 32 (1992).
3. S. Chandrasekhar, in *Hydrodynamic and Hydromagnetic Stability*, International Series of Monographs on Physics (Clarendon Press, Oxford, 1961).
4. T. R. Boehly, D. L. Brown, R. S. Craxton, R. L. Keck, J. P. Knauer, J. H. Kelly, T. J. Kessler, S. A. Kumpan, S. J. Loucks, S. A. Letzring, F. J. Marshall, R. L. McCrory, S. F. B. Morse, W. Seka, J. M. Soures, and C. P. Verdon, Opt. Commun. **133**, 495 (1997).
5. S. Skupsky, R. W. Short, T. Kessler, R. S. Craxton, S. Letzring, and J. M. Soures, J. Appl. Phys. **66**, 3456 (1989).
6. Y. Lin, T. J. Kessler, and G. N. Lawrence, Opt. Lett. **20**, 764 (1995).
7. T. R. Boehly, V. A. Smalyuk, D. D. Meyerhofer, J. P. Knauer, D. K. Bradley, R. S. Craxton, M. J. Guardalben, S. Skupsky, and T. J. Kessler, J. Appl. Phys. **85**, 3444 (1999).
8. V. N. Goncharov, J. P. Knauer, P. W. McKenty, P. B. Radha, T. C. Sangster, S. Skupsky, R. Betti, R. L. McCrory, and D. D. Meyerhofer, Phys. Plasmas **10**, 1906 (2003).
9. J. P. Knauer, K. Anderson, R. Betti, T. J. B. Collins, V. N. Goncharov, P. W. McKenty, D. D. Meyerhofer, P. B. Radha, S. P. Regan, T. C. Sangster, V. A. Smalyuk, J. A. Frenje, C. K. Li, R. D. Petrasso, and F. H. Séguin, Phys. Plasmas **12**, 056306 (2005).
10. N. Ohnishi *et al.*, J. Quant. Spectrosc. Radiat. Transf. **71**, 551 (2001).
11. S. P. Obenschain *et al.*, Phys. Plasmas **9**, 2234 (2002).
12. A. N. Mostovych, D. G. Colombant, M. Karasik, J. P. Knauer, A. J. Schmitt, and J. L. Weaver, Phys. Rev. Lett. **100**, 075002 (2008).
13. V. N. Goncharov, T. C. Sangster, P. B. Radha, R. Betti, T. R. Boehly, T. J. B. Collins, R. S. Craxton, J. A. Delettrez, R. Epstein, V. Yu. Glebov, S. X. Hu, I. V. Igumenshchev, J. P. Knauer, S. J. Loucks, J. A. Marozas, F. J. Marshall, R. L. McCrory, P. W. McKenty, D. D. Meyerhofer, S. P. Regan, W. Seka, S. Skupsky, V. A. Smalyuk, J. M.

Soures, C. Stoeckl, D. Shvarts, J. A. Frenje, R. D. Petrasso, C. K. Li, F. Séguin, W. Manheimer, and D. G. Colombant, Phys. Plasmas **15**, 056310 (2008).

14. R. Betti, V. N. Goncharov, R. L. McCrory, and C. P. Verdon, Phys. Plasmas **5**, 1446 (1998).

15. D. K. Bradley, P. M. Bell, O. L. Landen, J. D. Kilkenny, and J. Oertel, Rev. Sci. Instrum. **66**, 716 (1995).

16. V. A. Smalyuk, T. R. Boehly, L. S. Iwan, T. J. Kessler, J. P. Knauer, F. J. Marshall, D. D. Meyerhofer, C. Stoeckl, B. Yaakobi, and D. K. Bradley, Rev. Sci. Instrum. **72**, 635 (2001).

17. P. B. Radha, V. N. Goncharov, T. J. B. Collins, J. A. Delettrez, Y. Elbaz, V. Yu. Glebov, R. L. Keck, D. E. Keller, J. P. Knauer, J. A. Marozas, F. J. Marshall, P. W. McKenty, D. D. Meyerhofer, S. P. Regan, T. C. Sangster, D. Shvarts, S. Skupsky, Y. Srebro, R. P. J. Town, and C. Stoeckl, Phys. Plasmas **12**, 032702 (2005).

18. J. P. Knauer, R. Betti, D. K. Bradley, T. R. Boehly, T. J. B. Collins, V. N. Goncharov, P. W. McKenty, D. D. Meyerhofer, V. A. Smalyuk, C. P. Verdon, S. G. Glendinning, D. H. Kalantar, and R. G. Watt, Phys. Plasmas **7**, 338 (2000).

19. V. A. Smalyuk, S. X. Hu, J. D. Hager, J. A. Delettrez, D. D. Meyerhofer, T. C. Sangster, and D. Shvarts, Phys. Rev. Lett. **103**, 105001 (2009).

20. I. V. Igumenshchev, D. H. Edgell, V. N. Goncharov, J. A. Delettrez, A. V. Maximov, J. F. Myatt, W. Seka, A. Shvydky, S. Skupsky, and C. Stoeckl, Phys. Plasmas **17**, 122708 (2010).

21. S. X. Hu, G. Fiksel, V. N. Goncharov, S. Skupsky, D. D. Meyerhofer, and V. A. Smalyuk, "Mitigating Laser Imprints in Direct-Drive ICF Implosions with High-*Z* Dopants," submitted to Physical Review Letters.

22. V. A. Smalyuk, T. R. Boehly, D. K. Bradley, V. N. Goncharov, J. A. Delettrez, J. P. Knauer, D. D. Meyerhofer, D. Oron, and D. Shvarts, Phys. Rev. Lett. **81**, 5342 (1998).

23. V. A. Smalyuk, O. Sadot, J. A. Delettrez, D. D. Meyerhofer, S. P. Regan, and T. C. Sangster, Phys. Rev. Lett. **95**, 215001 (2005).